

accepted for publication in ApJL

Saturation and Thermalization of the Magnetorotational Instability: Recurrent Channel Flows and Reconnections

Takayoshi Sano¹ and Shu-ichiro Inutsuka^{2,3}

ABSTRACT

The nonlinear evolution and the saturation mechanism of the magnetorotational instability (MRI) are investigated using three-dimensional resistive MHD simulations. A local shearing box is used for our numerical analysis and the simulations begin with a purely vertical magnetic field. We find that the magnetic stress in the nonlinear stage of the MRI is strongly fluctuating. The time evolution shows the quasi-periodic recurrence of spike-shape variations typically for a few orbits which correspond to the rapid amplification of the magnetic field by the nonlinear growth of a two-channel solution followed by the decay through magnetic reconnections. The increase rate of the total energy in the shearing box system is analytically related to the volume-averaged torque in the system. We find that at the saturated state this energy gain of the system is balanced with the increase of the thermal energy mostly due to the joule heating. The spike-shape time evolution is a general feature of the nonlinear evolution of the MRI in the disks threaded by vertical fields and can be seen if the effective magnetic Reynolds number is larger than about unity.

Subject headings: accretion, accretion disks — diffusion — instabilities — MHD — turbulence

1. INTRODUCTION

The understanding of the origin of angular momentum transport has been required for the development of accretion disk theory. Balbus & Hawley (1991) have shown that weakly magnetized accretion disks are subject to a powerful local MHD instability. The discovery of this magnetorotational instability (MRI) brought about huge progress in the theoretical picture of accretion disks. Numerical simulations have revealed that the nonlinear evolution of the MRI

¹Department of Astronomy, University of Maryland, College Park, MD 20742-2421; sano@astro.umd.edu

²National Astronomical Observatory, Mitaka, Tokyo 181-8588, Japan

³Current address: Department of Physics, Kyoto University, Kyoto 606-8502, Japan

leads to MHD turbulence in which angular momentum is transported by the Maxwell stress (e.g., Hawley, Gammie, & Balbus 1995). Because the saturation amplitude of the stress determines the structure and evolution of the disks, the mechanism of the nonlinear saturation has a great importance for the theory. However the mechanism which regulates the saturation amplitude of the MHD turbulence is still unclear.

The purpose of this letter is to examine what is happening at the saturated turbulent state in order to find a clue to the understanding of the saturation mechanism. A local shearing box approximation is used for our numerical calculations so the evolution of the instability can be followed for many orbital periods. According to previous numerical studies, the saturation amplitudes of the Maxwell stress take similar values for both local and global disk calculations (e.g., Stone et al. 1996). Thus we should find the essential processes of the saturation mechanism in the local shearing box simulations.

The calculations include the effect of ohmic dissipation. Local 3D simulations show the nonlinear saturation of the MRI for both with and without the magnetic resistivity (Matsumoto & Tajima 1995; Fleming, Stone, & Hawley 2000). In axisymmetric 2D ideal MHD simulations with initially uniform vertical field, the evolution of the MRI results in an exponentially growing solution (two-channel flow) with no nonlinear saturation (Hawley & Balbus 1992). When the effect of ohmic dissipation is efficient enough, however, the nonlinear saturation occurs even in 2D (Sano, Inutsuka, & Miyama 1998). These results suggest that the resistivity is an important quantity in determining the saturated state. In this letter we focus on the effect of ohmic dissipation in 3D calculations. This approach has an advantage of reducing the influence of numerical dissipation on the saturated state that is characterized by the physical (i.e., ohmic) dissipation process.

2. NUMERICAL CALCULATIONS

The resistive MHD equations are solved by using a finite-difference code developed by Sano, Inutsuka, & Miyama (1999). We use the local shearing box approximation described in detail by Hawley et al. (1995). The Cartesian coordinate (x, y, z) is defined around the fiducial point comoving with a fiducial angular velocity Ω . Initially all the physical quantities are spatially uniform ($\rho = \rho_0$ and $P = P_0$, where ρ_0 and P_0 are constant) except for the azimuthal velocity $v_y(x) = -q\Omega x$, where $q = 3/2$ for a Keplerian disk. In this letter, we focus on an initial magnetic field configuration with a uniform vertical field, $B_z = B_{z0}$, although the nonlinear evolution of the MRI are affected by the field geometries (e.g., Fleming et al. 2000).

We choose normalizations with $\rho_0 = 1$, $\Omega = 10^{-3}$ and the computational box has radial size $L_x = 1$, azimuthal size $L_y = 4$, and vertical size $L_z = 1$. Most of the runs use a standard grid resolution of $32 \times 128 \times 32$. The initial characteristic wavelength of the MRI is given by $\lambda_{\text{MRI}} = 2\pi v_{Az0}/\Omega$ for the ideal MHD case (Balbus & Hawley 1991), where $v_{Az0} = B_{z0}/\sqrt{4\pi\rho_0}$ is the Alfvén speed. Its ratio to the vertical box size is assumed to be $\lambda_{\text{MRI}}/L_z = 0.32$ for all models.

Then the initial field strength of the models is $v_{Az0} = 5.0 \times 10^{-5}$. Note that the net flux associated with the initial vertical field remains unchanged in the time evolution even if the resistivity is included. We assume the initial ratio of the gas and magnetic pressure is $\beta_0 \equiv P_0/(B_{z0}^2/8\pi) = 10^4$, then the initial gas pressure is $P_0 = 1.25 \times 10^{-5}$ and the sound speed is $c_{s0} = 4.56 \times 10^{-3}$ with $\gamma = 5/3$. The magnetic diffusivity η is assumed to be constant and characterized by the magnetic Reynolds number Re_M . We define the magnetic Reynolds number as $Re_M = VL/\eta \equiv v_{Az0}^2/\eta\Omega$ using typical velocity $V = v_{Az0}$ and typical length scale $L = v_{Az0}/\Omega$.

3. LONG TIME EVOLUTIONS OF THE MRI

The efficiency of angular momentum transport is given by the turbulent shear stress, $w_{xy} = -B_x B_y / 4\pi + \rho v_x \delta v_y$, where the first and second terms are the Maxwell and Reynolds stress, respectively, and $\delta v_y \equiv v_y + q\Omega x$. Figure 1 shows the time evolutions of volume-averaged Maxwell stress, $\langle -B_x B_y / 4\pi \rangle$.⁴ The top panel is the result of the case with $Re_M = 1$ and the bottom is of the ideal MHD ($\eta = 0$) case.

The Maxwell stress dominates the Reynolds stress throughout the turbulent stage by a factor of about 6. The stress of the nonlinear stage is highly fluctuating for both cases shown in Figure 1. The main feature of the time evolutions is the many spike-shape excursions in the stress. Power spectral density declines with frequency w approximately as w^{-2} at frequencies above a few orbital period, and almost flat at lower frequencies. Note that the break point corresponds to the typical timescale of the spike.

The time averages of the Maxwell stress are shown in Figure 1 by dotted lines and they are $0.024 P_0$ and $0.013 P_0$ for the $Re_M = 1$ and $\eta = 0$ runs. Because the contribution of the spike-shape variations to the average is large, the understanding of the time evolution of these spikes is essential to estimate the saturation amplitude of the stress.

The diffusion length $l_{\text{diff}} \equiv \eta/v_{Az0} = 0.05$ is larger than the grid scale $l_{\text{grid}} = 1/32 = 0.03$ for the $Re_M = 1$ run, so that we can resolve the physical effect of the resistivity. In the ideal MHD run, on the other hand, the dissipation of the magnetic field is due to artificial numerical effects (Hawley et al. 1995). Although the resemblance of the time evolutions between the $Re_M = 1$ and $\eta = 0$ runs might suggest that the numerical dissipation works in a similar way to the physical resistivity, we use the results of the $Re_M = 1$ run in the following discussions.

At the peak of each spike, a well-organized two-channel solution dominates in the entire computational box. Figure 2 shows images of the azimuthal component of the magnetic field, that is the dominant component at the saturated state. Top panel is the image at a time of the peak of a spike. The distribution is almost independent of x and y . The upper half of

⁴The single brackets $\langle f \rangle$ imply a volume average of quantity f . We also use double brackets $\langle\langle f \rangle\rangle$ to denote a time and volume average.

fluid has a strong horizontal field with positive B_x and negative B_y , and the lower half has the oppositely directed field with negative B_x and positive B_y . The perturbed velocity is nearly horizontal in the same direction as the fields but has the maximum at the neutral sheet of the fields. Because the gas pressure is still larger than the magnetic pressure by more than two orders of magnitude even at the nonlinear stage, the evolution is almost incompressible. Even at the maximum growth of the channel flow, the fluctuations of the density and pressure are very small, $\langle \delta \rho^2 \rangle^{1/2} / \langle \rho \rangle \sim 7.2 \times 10^{-3}$ and $\langle \delta P^2 \rangle^{1/2} / \langle P \rangle \sim 1.5 \times 10^{-2}$, compared with the fluctuation of the magnetic pressure, $\langle \delta P_{\text{mag}}^2 \rangle^{1/2} / \langle P_{\text{mag}} \rangle \sim 0.75$. The exponentially growing channel solution is an exact solution for nonlinear incompressible MHD equations, thus the horizontal fields are amplified up to $|B_x|_{\text{max}} \sim 18B_{z0}$ and $|B_y|_{\text{max}} \sim 30B_{z0}$ by this nonlinear growth. The perturbed velocity is of the order of the Alfvén speed at this time and is still subsonic; $\langle |\delta v| \rangle \sim 0.56 \langle v_A \rangle \sim 0.073 \langle c_s \rangle$.

The image at a time just after the peak is shown in the middle panel of Figure 2. The channel flow is known to be unstable for the parasitic instability (Goodman & Xu 1994). Because the growth rate is proportional to the amplitude of the channel solution, this instability appears after the sufficient growth of the two-channel flow. The unstable modes have finite k_x and k_y and their wavelength $2\pi/(k_x^2 + k_y^2)^{1/2}$ must be longer than the vertical length of the channel L_z . This kind of pattern occurs in the image of the spatial distribution of the magnetic field. The parasitic instability generates vertical motions and gives a chance for oppositely directed magnetic fields to approach each other. Then the dissipation of the magnetic field takes place efficiently through the magnetic reconnections. Finally the channel flow disappears and a disorganized MHD turbulence lasts until the next channel flow starts growing (bottom panel of Fig. 2). The magnetic energy is an order of magnitude smaller than the peak value and is almost equi-partitioned with the perturbed kinetic energy; $\langle |\delta v| \rangle \sim 0.83 \langle v_A \rangle \sim 0.053 \langle c_s \rangle$.

4. ENERGY BUDGET IN THE MHD TURBULENCE

According to Hawley et al. (1995), we define the total energy within the shearing box as

$$\Gamma \equiv \int d^3x \left[\rho \left(\frac{v^2}{2} + \epsilon + \phi \right) + \frac{B^2}{8\pi} \right], \quad (1)$$

where ϵ means the specific internal energy and $\phi = -q\Omega^2 x^2$ is the tidal expansion of the effective potential. Using the evolution equation for the resistive MHD system, the time-derivative of the above equation gives

$$\frac{d\Gamma}{dt} = q\Omega L_x \int_X dA \left(\rho v_x \delta v_y - \frac{B_x B_y}{4\pi} \right), \quad (2)$$

where dA is the surface element and the integral is taken over either of the radial boundary. Thus the increase rate of the total energy is proportional to the stress w_{xy} at the radial boundary. Balbus & Papaloizou (1999) have shown that the similar relation in the cylindrical coordinates holds for the global disk problem. Although the final expression of equation (2) does not explicitly

depend on the amount of resistivity, the joule heating is crucial for the transformation of the magnetic energy into the thermal energy (see below).

Using the volume-averaged stress $\langle w_{xy} \rangle$ instead of the surface-averaged value of the stress at the radial boundary $\langle w_{xy} \rangle_X$, the volume average of the input energy $\langle \dot{E}_{\text{in}} \rangle$ is approximately given by

$$\langle \dot{E}_{\text{in}} \rangle \equiv \frac{\partial \langle E_{\text{in}} \rangle}{\partial t} = q\Omega \langle w_{xy} \rangle_X \approx q\Omega \langle w_{xy} \rangle . \quad (3)$$

Because our numerical scheme solves the energy equation in terms of the total energy, our calculations perfectly satisfy equation (2). Furthermore, the density does not vary much so that the change in potential energy $\rho\phi$ is negligible compared with the other terms in equation (1). Thus the input energy E_{in} is almost identical to the increase of the sum of $E_{\text{th}} = \rho\epsilon = P/(\gamma - 1)$, $E_{\text{mag}} = B^2/8\pi$, and $E_{\text{kin}} = \rho v^2/2$. This is clearly shown in Figure 3 which depicts the time evolutions of $\langle \dot{E}_{\text{in}} \rangle$ and $\langle \dot{E}_{\text{tot}} \rangle \equiv \langle \dot{E}_{\text{th}} \rangle + \langle \dot{E}_{\text{mag}} \rangle + \langle \dot{E}_{\text{kin}} \rangle$. $\langle \dot{E}_{\text{in}} \rangle$ and $\langle \dot{E}_{\text{tot}} \rangle$ take such close values that their curves overlap each other.

The time evolution of $\langle \dot{E}_{\text{th}} \rangle$ is shown in Figure 3 by a dotted curve. Because $\langle \dot{E}_{\text{in}} \rangle$ is proportional to the Maxwell stress, its time evolution has spike-shape variations. As seen from the figure, the evolution of $\langle \dot{E}_{\text{th}} \rangle$ also has many spikes with the similar amplitude to $\langle \dot{E}_{\text{in}} \rangle$. The time average of $\langle \dot{E}_{\text{th}} \rangle$ takes almost the same value as that of $\langle \dot{E}_{\text{in}} \rangle$. The difference $|\langle \langle \dot{E}_{\text{th}} \rangle \rangle - \langle \langle \dot{E}_{\text{in}} \rangle \rangle|/\langle \langle \dot{E}_{\text{in}} \rangle \rangle$ is less than 10^{-2} , when we calculate the time averages from 10 to 25 orbits. Thus the energy gain of the system is finally transformed into the thermal energy. The thermal energy must be increasing throughout the nonlinear evolution unless some cooling process is included. The magnetic and kinetic energies, on the other hand, are saturated, thus the time averages of their rates of change are $\langle \langle \dot{E}_{\text{mag}} \rangle \rangle \sim \langle \langle \dot{E}_{\text{kin}} \rangle \rangle \sim 0$. This means that the time and spatial average of the energy gain $d\Gamma/dt$ should amount to the time and spatial average of the heating rate due to turbulent dissipation, provided the magnetic and kinetic energy are saturated. That is

$$\langle \langle \dot{E}_{\text{th}} \rangle \rangle \approx q\Omega \langle \langle w_{xy} \rangle \rangle . \quad (4)$$

Here we cannot remove the symbol $\langle \langle \rangle \rangle$ from this equation. In other words, this *fluctuation-dissipation relation* holds only in the coarse-grained description of the thermalization rate and the correlated fluctuation of magnetic field and velocity perturbations. Note that this equation does not hold in the 2D simulation with $Re_M \gtrsim 1$ where the system does not show the saturation.

Figure 4 shows the time evolutions of $\langle \dot{E}_{\text{in}} \rangle$, $\langle \dot{E}_{\text{th}} \rangle$, and $\langle \dot{E}_{\text{mag}} \rangle$ at a typical spike-shape variation. The joule heating rate $\langle \dot{E}_{\text{joule}} \rangle \equiv \eta |\nabla \times \mathbf{B}|^2/4\pi$ is also shown in this figure. The joule heating is about 80 percent of the thermal energy increase. (This fraction is almost 100 % for the $Re_M = 0.3$ run.) Throughout the nonlinear evolution, the magnetic energy is transformed into the thermal energy at a rate which over time matches $\langle \dot{E}_{\text{in}} \rangle$. Thus the saturation of the magnetic energy is achieved by a time-averaged balance between the energy gain by the growth of the MRI and the loss by the joule heating in the reconnection process.

We find that the peak in $\langle \dot{E}_{\text{th}} \rangle$ is always delayed from $\langle \dot{E}_{\text{in}} \rangle$, and that the sign of $\langle \dot{E}_{\text{mag}} \rangle$

changes around the peak in $\langle \dot{E}_{\text{th}} \rangle$. The kinetic energy has a similar time evolution to E_{mag} , but the amplitude of the fluctuations in $\langle \dot{E}_{\text{kin}} \rangle$ is negligible compared with that of the magnetic energy. The spike-shape variation of $\langle \dot{E}_{\text{in}} \rangle$ starts with the onset of a channel flow. The magnetic energy increases due to the growth of the MRI and $\langle \dot{E}_{\text{mag}} \rangle$ takes a positive peak value at the maximum growth of the two-channel solution, which corresponds to the peak in $\langle \dot{E}_{\text{in}} \rangle$ (top panel of Fig. 2). When the channel flow is destroyed by the parasitic instability, the large scale magnetic reconnections become efficient. Then the sign of $\langle \dot{E}_{\text{mag}} \rangle$ changes from positive to negative and the thermal energy increases rapidly. When the $\langle \dot{E}_{\text{mag}} \rangle$ takes a negative peak, $\langle \dot{E}_{\text{th}} \rangle$ is nearly at the top of the peak (middle panel of Fig. 2).

5. DEPENDENCE OF THE SATURATION CHARACTER ON THE MAGNETIC REYNOLDS NUMBER

We find that two-channel solutions appear repeatedly in nonlinear turbulent stage. The behavior similar to this appearance of a channel flow can be seen in 2D simulations, which show a two-channel flow appears at the end of the calculations even though the initial value of λ_{MRI} is smaller than the box size. This inverse cascade is characteristic of both 2D and 3D nonlinear evolutions of the MRI in the cases $Re_M \gtrsim 1$. The difference between 2D and 3D simulations is that in 3D the channel flow is unstable to non-axisymmetric modes of the parasitic instability. Then the question is why the two-channel solution appear in nonlinear stage of the MRI.

The key quantity is the characteristic length of the instability expected from the linear analysis. The most unstable wavelength of the MRI is given by $\lambda_{\text{MRI}} \sim v_A/\Omega \propto v_A$ for less resistive cases $Re_M \gtrsim 1$. If the field is amplified by the growth of the MRI, then λ_{MRI} shifts to the longer wavelength. Therefore it can reach the vertical box size, and the longest wavelength mode, a two-channel solution, appears finally in nonlinear evolution. This is the reason for the inverse cascade. For $Re_M \lesssim 1$, on the other hand, the characteristic wavelength is given by $\lambda_{\text{MRI}} \sim \eta/v_A \propto v_A^{-1}$ (Sano & Miyama 1999). Thus the wavelength λ_{MRI} becomes shorter when the field is amplified. In fact, 2D simulations with $Re_M \lesssim 1$ show that the saturated state is a disorganized MHD turbulence and no emergence of a two-channel flow (Sano et al. 1998). We find this is true even for 3D cases. For the case with $Re_M = 0.3$, the nonlinear evolution shows no growth of a two-channel flow. The amplitude of the time variability of the Maxwell stress is very small in this case. Due to the lack of the nonlinear growth of the channel flow, the horizontal component of the magnetic energy is not amplified very much and remains only 2 times larger than the vertical, while this ratio $\langle\langle B_y^2 \rangle\rangle / \langle\langle B_z^2 \rangle\rangle$ is an order of magnitude larger for $Re_M \gtrsim 1$ cases. The energy balance at the saturated state is roughly given by $\langle\langle \dot{E}_{\text{in}} \rangle\rangle \sim \langle\langle \dot{E}_{\text{th}} \rangle\rangle \sim \langle\langle \dot{E}_{\text{joule}} \rangle\rangle$ same as in the cases with $Re_M \gtrsim 1$. Because the diffusion time is comparable to the growth time of the MRI in this case, the magnetic diffusion would be an important process for the joule heating as well as the recurrent and rapid magnetic reconnections. The saturation amplitude is two orders of magnitude smaller than the models with $Re_M \gtrsim 1$, so that the angular momentum transport by

the MRI is not efficient when $Re_M \lesssim 1$.

We can categorize the saturated states of the MRI into two types when the disks are threaded by uniform vertical fields initially. The first type involves the recurrence of the channel flow and large scale reconnections (the $Re_M = 1$ and ideal MHD runs). In the disorganized MHD turbulence of the second type, the magnetic diffusion and reconnections prevail without the significant growth of the channel flow (the $Re_M = 0.3$ run). The angular momentum transport by the magnetic stress is efficient only for the first type. The difference of these two types is caused by the different dependence of the characteristic length of the MRI, λ_{MRI} , on the magnetic field strength. Thus the magnetic Reynolds number defined as $Re_M = v_A^2/\eta\Omega$ can characterize the linear and nonlinear features of the MRI and the critical value is $Re_M \sim 1$.

We thank James Stone and Neal Turner for useful discussions. Computations were carried out on the VPP5000 at the National Astronomical Observatory of Japan and the VPP700 at the Subaru Telescope, NAOJ.

REFERENCES

Balbus, S. A., & Hawley, J. F. 1991, ApJ, 376, 214

Balbus, S. A., & Papaloizou, J. C. 1999, ApJ, 521, 650

Fleming, T. P., Stone, J. M., & Hawley, J. F. 2000, ApJ, 530, 464

Goodman, J., & Xu, G. 1994, ApJ, 432, 213

Hawley, J. F., & Balbus, S. A. 1992, ApJ, 400, 595

Hawley, J. F., Gammie, C. F., & Balbus, S. A. 1995, ApJ, 440, 742

Matsumoto, R., & Tajima, T. 1995, ApJ, 445, 767

Sano, T., Inutsuka, S., & Miyama, S. M. 1998, ApJ, 506, L57

Sano, T., Inutsuka, S., & Miyama, S. M. 1999, in Numerical Astrophysics, ed. S. M. Miyama, K. Tomisaka, & T. Hanawa (Dordrecht: Kluwer), 383

Sano, T., & Miyama, S. M. 1999, ApJ, 515, 776

Stone, J. M., Hawley, J. F., Gammie, C. F., & Balbus, S. A. 1996, ApJ, 463, 656

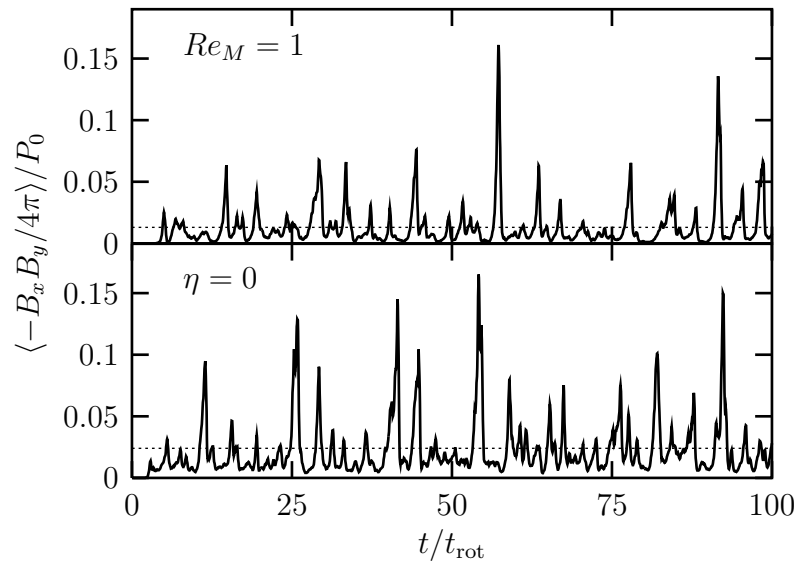


Fig. 1.— Time evolution of volume-averaged Maxwell stress for the model with $Re_M = 1$ (top) and $\eta = 0$ (bottom). Time is given in the rotation time $t_{\text{rot}} = 2\pi/\Omega$. Dotted lines show their time-averaged values done from 10 to 100 orbits. The grid resolution of these runs is $32 \times 128 \times 32$.

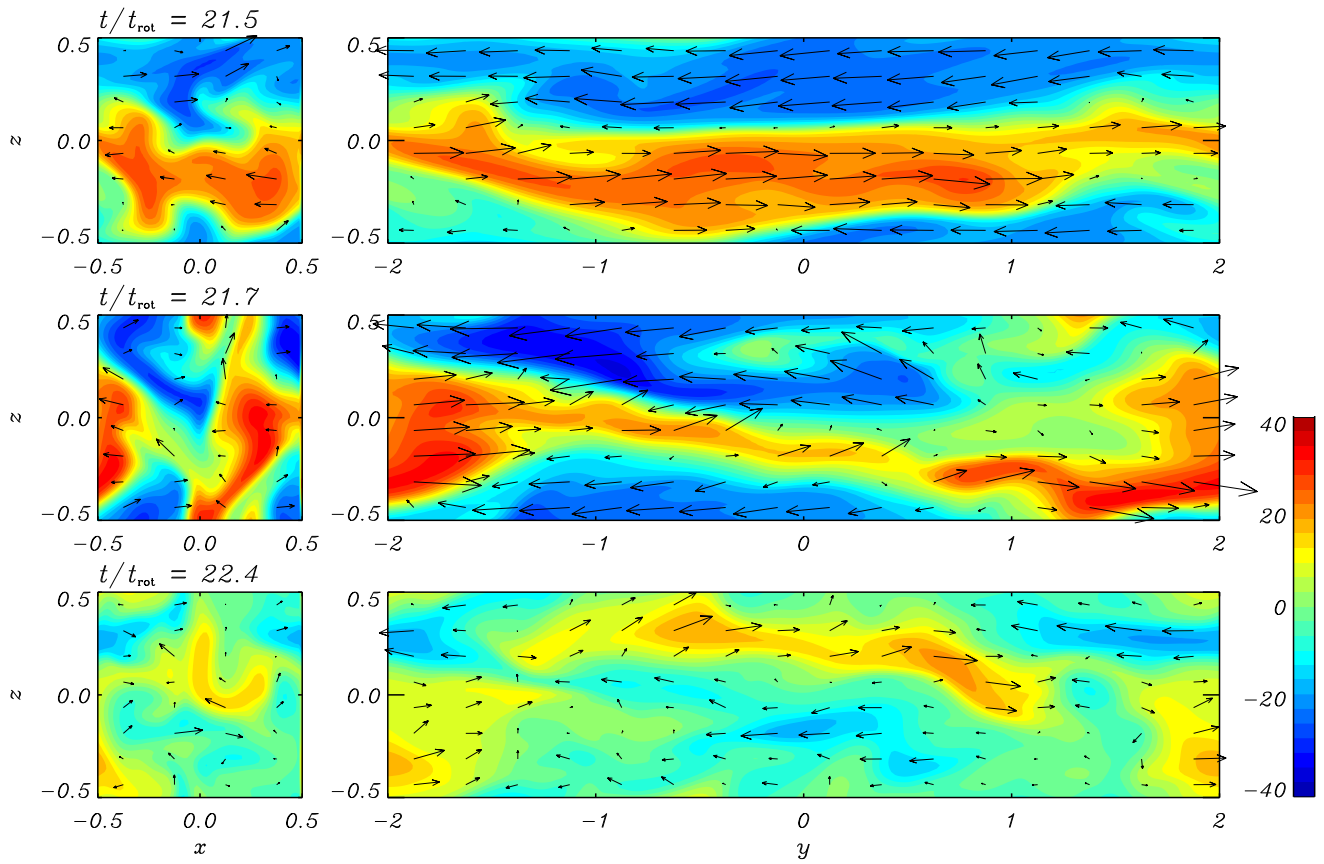


Fig. 2.— Slices in the x - z plane at $y = -2$ and in the y - z plane at $x = -0.5$ of the azimuthal component of the magnetic fields B_y/B_{z0} (colors) and magnetic field vectors (arrows) in the $Re_M = 1$ run with grid resolution $64 \times 256 \times 64$. From top to bottom the time of the image is $t/t_{\text{rot}} = 21.5, 21.7$, and 22.4 .

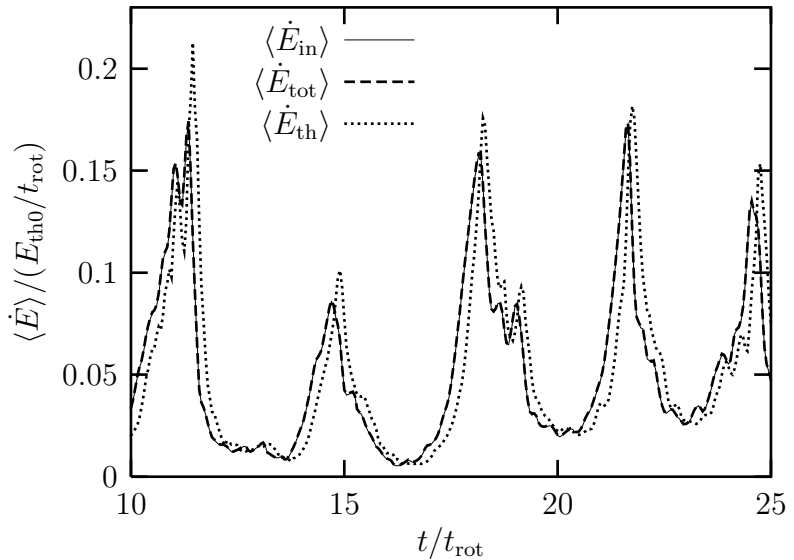


Fig. 3.— Time evolution of volume-averaged time derivative of input energy $\langle \dot{E}_{\text{in}} \rangle$, total energy $\langle \dot{E}_{\text{tot}} \rangle \equiv \langle \dot{E}_{\text{th}} \rangle + \langle \dot{E}_{\text{mag}} \rangle + \langle \dot{E}_{\text{kin}} \rangle$, and thermal energy $\langle \dot{E}_{\text{th}} \rangle$ of the $Re_M = 1$ run with grid resolution $64 \times 256 \times 64$. The time derivatives of the energies are given in units of $E_{\text{th}0}/t_{\text{rot}}$ where $E_{\text{th}0} = P_0/(\gamma - 1)$ is the initial thermal energy.

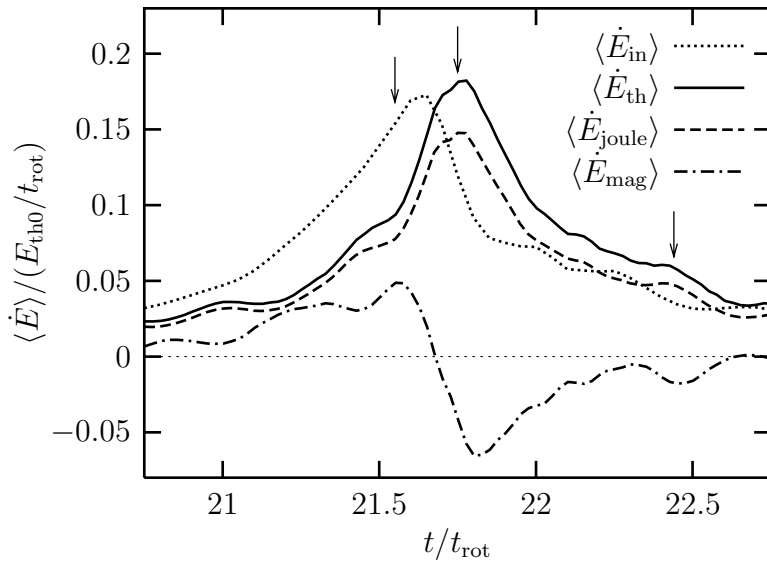


Fig. 4.— Time evolution of volume-averaged time derivative of input energy $\langle \dot{E}_{in} \rangle$, thermal energy $\langle \dot{E}_{th} \rangle$, and magnetic energy $\langle \dot{E}_{mag} \rangle$ and volume-averaged joule heating rate $\langle \dot{E}_{joule} \rangle$ at a spike-shape variation in $Re_M = 1$ run with grid resolution $64 \times 256 \times 64$. Arrows denote the times of the snapshots shown in Figure 2.